Ionics (2019) 25:5105–5115
https://doi.org/10.1007/s11581-019-03088-0

ORIGINAL PAPER

Cobalt-doped $Ca_{12}Al_{14}O_{33}$ mayenite oxide ion conductors: phases, defects, and electrical properties

Huaibo Yi[1] · Yun Lv[1] · Victoria Mattick[2] · Jungu Xu[1]

Received: 26 March 2019 / Revised: 5 May 2019 / Accepted: 23 May 2019 / Published online: 18 June 2019

Abstract

Mayenite $Ca_{12}Al_{14}O_{33}$, as a good oxygen ion conductor with conductivity slightly lower than stabilized ZrO_2, has been investigated through doping strategy over the last few decades, but with little success in further improving its oxide ionic conductivity. Here, cobalt-doped $Ca_{12}Al_{14-x}Co_xO_{33+\delta}$ $(0 \le x \le 1.6)$ materials were prepared by traditional solid-state reaction method, and then studied by complementary techniques, including X-ray diffraction (XRD), scanning electron microscope coupled with energy dispersion spectrum (EDS) analysis, X-ray photoelectron spectroscopy, and static lattice atomistic simulations. The results showed that these doped materials had much lower Co contents in the crystal structure than their nominal compositions, which was consistent with the high calculated defect formation energy (~ 6.25 eV). The minor divalent Co ions in the crystal structure would reduce the amount of mobile oxide ions and accordingly slightly decreased the bulk conductivities, while most of the Co ions existed in the form of Co_2O_3 and segregated along grain boundaries in the ceramic samples, which could apparently increase the grain boundary conductions of $Ca_{12}Al_{14}O_{33}$.

Keywords Oxide ion conductor · $Ca_{12}Al_{14}O_{33}$ mayenite · Rietveld refinement · Static lattice atomistic simulation

Introduction

Solid oxide fuel cells (SOFCs), as a clean energy conversion technology with high efficiency and fuel flexibility, are gaining increased attention over the last few decades [1–3]. Oxide ion–conducting electrolyte plays a crucial role in the working temperature range of SOFCs [4–6]. The yttrium-stabilized ZrO_2 (YSZ), as a traditional and most widely used electrolyte in the industry, can be used only for temperatures higher than 750 °C [7–9]. This high working temperature raises undesired reactions between the electrolyte and electrode materials as well as issues concerning thermal stresses. Thus, it is important to develop new oxide ion conductors with high ionic conductivity for SOFCs subjected to intermediate temperatures (500–750 °C) [9–11].

The oxide ion conductivity of mayenite $Ca_{12}Al_{14}O_{33}$ was first identified in 1988 by M. Lacerda et al. [12]. The $Ca_{12}Al_{14}O_{33}$ material possesses slightly lower oxide ion conduction than that of YSZ, which therefore makes $Ca_{12}Al_{14}O_{33}$ a competitive candidate for SOFC electrolytes. The parent $Ca_{12}Al_{14}O_{33}$ has a cubic crystal structure belonging to the $I\bar{4}3d$ space group with a lattice constant of ~ 11.99 Å. For each unit cell, there are two $Ca_{12}Al_{14}O_{33}$ molecules. Twelve cages build up the positively charged framework, with two free O ions randomly occupying two different cages. The unit cell can therefore be represented by a chemical formula $[Ca_{24}Al_{28}O_{64}]^{4+}\bullet 2O^{2-}$. Each cage that composed of framework Ca, Al, and O atoms has a width of ~ 6 Å and surrounded by 8 other cages with ~ 3.7 Å wide windows shared, as shown in Fig. 1. The highly mobile free oxygen ions lead already for the parent $Ca_{12}Al_{14}O_{33}$ material to an oxide ion conductor. The oxygen migration in un-doped $Ca_{12}Al_{14}O_{33}$ material was examined by neutron diffraction [13], density functional theory (DFT), and molecular dynamics (MD) calculations [14, 15] as well as oxygen-isotope-

---

✉ Victoria Mattick
vikimattick@gmail.com

✉ Jungu Xu
xujungu@glut.edu.cn

[1] MOE Key Laboratory of New Processing Technology for Nonferrous Metals and Materials, Guangxi Universities Key Laboratory of Non-ferrous Metal Oxide Electronic Functional Materials and Devices, College of Materials Science and Engineering, Guilin University of Technology, Guilin 541004, People's Republic of China

[2] Department of Chemical Engineering, University of South Carolina, Columbia, SC 29201, USA

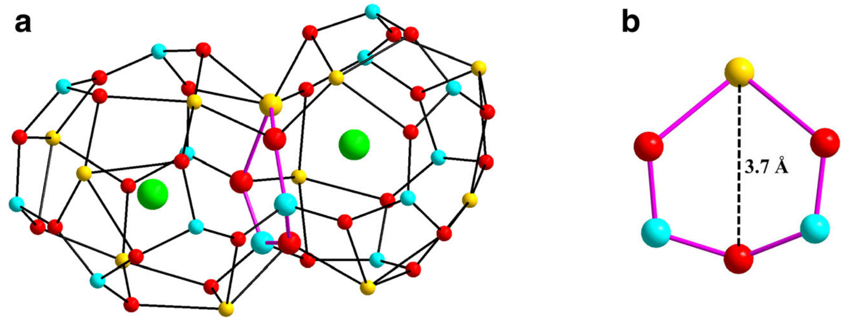

Fig. 1 **a** Two exemplar connecting cages; **b** the window shared by two adjacent cages in $Ca_{12}Al_{14}O_{33}$. The green, cyan, yellow, and red balls represent free oxygen, framework Al, Ca, and O atoms, respectively; the value "3.7 Å" denotes the width of the window, which is exactly the longest distance between Ca and O atoms in this window

exchange experiments [16, 17]. Irvine et al. made the first attempt to enhance the high-temperature ionic conduction of $Ca_{12}Al_{14}O_{33}$ material by zinc doping or zinc and phosphorus co-doping on the Al sites [18]. Then, Ebbinghaus et al. investigated the iron-doped mayenite [19]. Both of these cases resulted in slight decreases in ionic conduction for the doped samples. Studies of copper [20] or iridium [21] incorporation into mayenite were also reported, without effects of these dopants on the oxide ion conduction being examined. More recently, we reported the synthesis, defects, and electrical properties of Ga-doped $Ca_{12}Al_{14}O_{33}$ material [22]. Ga-doping on the Al site was shown to improve the bulk conductivity of $Ca_{12}Al_{14}O_{33}$.

In this study, the Co ions, which have larger ionic sizes than the Al ions in the same coordination environment, were selected to substitute for Al in order to increase the lattice parameters and enlarge the width of the window of two connecting neighboring cages, which will accordingly benefit the migration of oxide ions. The effects of Co doping on the phase, structure, and electrical properties of $Ca_{12}Al_{14}O_{33}$ were then investigated. The results show that the raw material Co_2O_3 mainly existed as a secondary phase in the product and segregated along the grain boundaries of $Ca_{12}Al_{14}O_{33}$, which could apparently increase the grain boundary conduction, especially at temperatures below 700 °C. Only a small part of Co_2O_3 was reduced at high temperature into divalent Co^{2+} ions. These divalent Co^{2+} ions can successfully substitute the 4-coordinated Al ions in $Ca_{12}Al_{14}O_{33}$. However, this acceptor-doping would lead to a slight decrease in the bulk conductivity of $Ca_{12}Al_{14}O_{33}$, which may due to the decrease of free oxygen that caused by the acceptor-doping. The high defect formation energy for Co^{2+} ions substituting for 4-coordinated tetrahedral Al ions derived from the static lattice simulation agreed well with its narrow solid solution range.

Materials and methods

The samples of $Ca_{12}Al_{14-x}Co_xO_{33+\delta}$ were prepared by a traditional solid-state reaction method using $CaCO_3$ (Alfa Aesar, > 99.8% purity), Al_2O_3 (Alfa Aesar, > 99.997% purity), and Co_2O_3 (Alfa Aesar, > 99.99% purity) as starting raw materials. All raw materials were weighed stoichiometrically. The evenly mixed and well-ground raw materials were first fired at 1000 °C for 12 h to drive off CO_2. The precalcined powders, after regrinding, were then uniaxially pressed into pellets and sintered at 1250 °C for 24 h in the air to make the reaction fully completed and yield the target products. Archimedes principle was applied to estimate the densities of these prepared ceramics.

The XRD characterizations were performed on a Panalytical X'pert Pro X-ray diffractometer with Cu Kα radiation. For Rietveld refinement applications, the XRD data were collected over a 2θ range of 5–120°. Topas-Academic software [23] was used for these refinements. X-ray photoelectron spectroscopy (XPS) was recorded on ESCALAB 250Xi, Thermo Scientific (America), and a vacuum of 10^{-10} mbar was applied. The microstructure and EDS analyses were performed on a Hitachi (Tokyo, Japan) S4800 scanning electron microscope (SEM). Solartron 1260 frequency response analyzer was used to perform the AC impedance spectroscopy (IS) measurements over a 10^7–10^{-1} Hz frequency range. Prior to performing the IS measurements, the platinum paste was coated on the opposite faces of the pellets and subsequently fired at 750 °C for 1 h to remove organic components and form electrodes.

The energies of Co^{2+} ions substituting for Al^{3+} ions were studied by atomistic static lattice simulations, using the General Utility Lattice Program (GULP) [24, 25] based on the interatomic potential approach. Buckingham potential function [26] was used to model the interactions between ions, using the shell model [27] to describe the electronic polarizability for structural modeling. The interatomic potential parameters used for the atomistic simulations are listed in Table 1.

Results and discussion

XRD data

Figure 2a shows the XRD patterns of $Ca_{12}Al_{14-x}Co_xO_{33+\delta}$ ($0 \leq x \leq 1.6$). We can clearly see that no peaks from a secondary phase are observed for compositions $x \leq 1.2$, and all the

Table 1 Buckingham interatomic potential and shell model parameters used for the atomistic simulations

Interaction	*A* (eV)	*ρ* (Å)	*C* (eV Å^6)	*Y* (e)	*k* (eV Å^{-2})
Ca^{2+}–O^{2-}	1227.7	0.3372	0.0	0	–
Al^{3+}–O^{2-}	1474.4	0.3006	0.0	1.458	1732.0
Co^{2+}–O^{2-}	778.02	0.3301	0.0	0	–
Co^{3+}–O^{2-}	1329.82	0.3087	0.0	2.04	196.3
O^{2-}–O^{2-}	9547.96	0.2191	32	− 2.869	42.0

Buckingham potential: $V_{ij}(r_{ij}) = A\exp(2r_{ij}/\rho) - C/r_{ij}^6$, where r_{ij} is the distance between ions *i* and *j*; the *A*, *ρ*, and *C* are empirically derived parameters which need to be determined in order to describe a specific ion–ion interaction; *Y* is the charge of the shell of an ion described by the shell model, while *k* is the harmonic spring between the core and shell of an ion

reflection peaks can be indexed with the mayenite structure phase $Ca_{12}Al_{14}O_{33}$ (PDF#70-2144). For $x = 1.6$, however, reflections from Co_2O_3 (PDF#02-0770) impurity appear. The refined cell parameters for different compositions were plotted in Fig. 2b which shows that the lattice parameters of the doped materials are close to each other and only slightly higher than that of the un-doped parent material, indicating deviations between the exactly Co contents in the crystal structure and the nominal compositions. According to Vegard's law [28], unit cell parameters should vary linearly with composition for a continuous substitutional solid solution. Here, as the effective ionic radius of Al^{3+} (in a four-coordinated environment) is ~ 0.39 Å, smaller than that of Co^{2+}/Co^{3+} (> 0.5 Å) [29], a linear lattice expansion obeying Vegard's law is expected for $Ca_{12}Al_{14\text{-}x}Co_xO_{33+\delta}$ with increasing values of *x*, if all the Co atoms enter into the crystal structure and occupy the Al atoms' sites. Rietveld structure refinements were then carried out on all these doped samples. For these Rietveld refinements, a parent cubic $Ca_{12}Al_{14}O_{33}$ structure (space group $I\bar{4}3d$) was used as the starting structure model. This model contains two Ca sites (24*d*), two Al sites (16*c* and 12*a*) in two different kinds of AlO_4 tetrahedron (3-linked and 4-linked, respectively, the numbers 3 and 4 denoting the bridging oxygen number of an AlO_4 tetrahedron corner-shared with other AlO_4 tetrahedra), and three oxygen sites (one 16*c* and two 48*e*). Results of refinements show that the Co contents in the crystal structure of all these doped samples are similar and that the Co atoms have a preferred distribution on the 3-linked Al2 site. The typical Rietveld fitted plot and the final refined structural parameters (including the Wyckoff site, fractional coordinate (*x*, *y*, *z*), occupancy, and isotropic thermal factor B_{iso}) of the $Ca_{12}Al_{12.8}Co_{1.2}O_{33+\delta}$ sample which has the highest nominal Co content (without secondary phases observed in the XRD patterns) are given in Fig. 3 and Table 2, respectively. The refined cell parameter $a = 11.9959(1)$ Å, weighted profile *R* factor $R_{wp} \approx 5.16\%$, Bragg-intensity *R* factor $R_B \approx 3.78\%$. Such low *R* factors indicate the good reliability of the refinement. The refined occupancy of Co on the 3-linked Al2 site is ~ 0.022(1), corresponding to the chemical formula $Ca_{12}Al_{13.824(4)}Co_{0.176(4)}O_{33+\delta}$. Therefore, the Co content in the crystal structure is believed to be much lower than that expected in the nominal formula. In fact, attempt to fix the

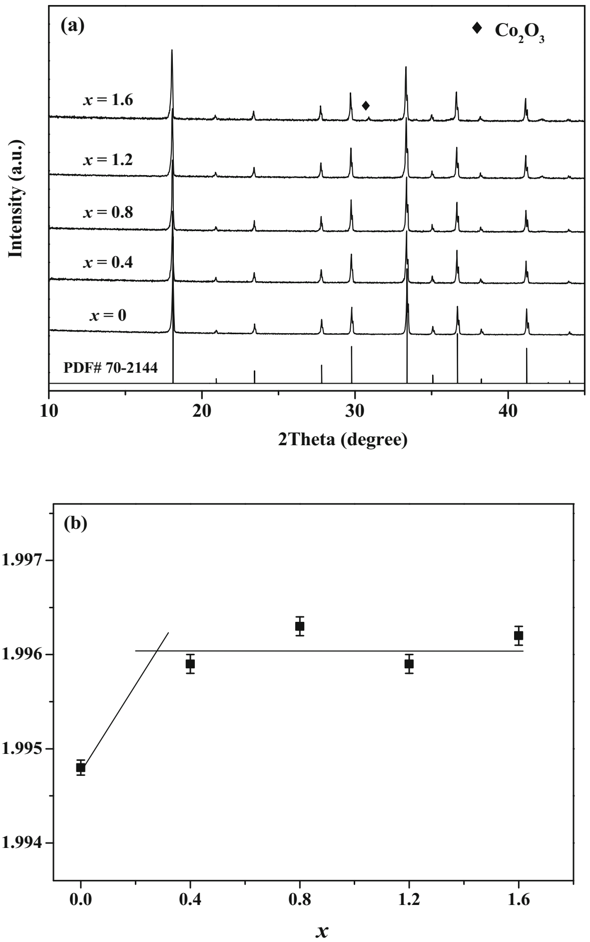

Fig. 2 **a** XRD patterns and **b** refined cell parameters with errors included of $Ca_{12}Al_{14\text{-}x}Co_xO_{33+\delta}$ ($x = 0$, 0.4, 0.8, 1.2, and 1.6)

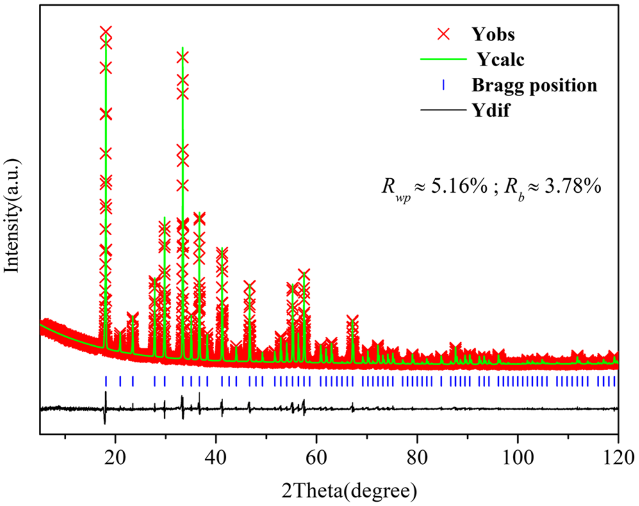

Fig. 3 Rietveld fitting for XRD data of $Ca_{12}Al_{12.8}Co_{1.2}O_{33+\delta}$

Table 2 Final refined structural parameters of $Ca_{12}Al_{12.8}Co_{1.2}O_{33+\delta}$

Atom	Wyckoff site	*x*	*y*	*z*	Occupancy	B_{iso}(Å^2)
Ca1	24*d*	0.1111(3)	0	1/4	0.844(2)	0.58(6)
Ca2	24*d*	0.059(1)	0	1/4	0.156(2)	0.31(2)
Al1	12*a*	3/8	0	1/4	1	0.77(4)
Al2	16*c*	− 0.0171(1)	− 0.0171(1)	− 0.0171(1)	0.978(1)	1.38(5)
Co1	16*c*	− 0.0171(1)	− 0.0171(1)	− 0.0171(1)	0.022(1)	1.38(5)
O1	16*c*	0.064(1)	0.064(1)	0.064(1)	1	1.4(1)
O2	48*e*	0.1023(2)	0.1916(3)	0.2887(1)	1	2.1(1)
O3	48*e*	0.2763(2)	0.111(1)	0.943(2)	0.0416(1)	1.6(3)

Lattice parameters: $a = 11.9959(1)$ Å, space group I$\bar{4}$ 3d, weighted profile *R* factor $R_{wp} \approx 5.16\%$, Bragg-intensity *R* factor $R_B \approx 3.78\%$

Co content in the crystal structure as high as designed would lead to a much worse fitting result with $R_{wp} > 18\%$. In addition, when we fixed all the Co atoms on the 4-linked Al site, the refinement also had a much worse result ($R_{wp} \approx 11\%$).

SEM analysis

As stated above, the refined Co content in the crystal structure is much lower than expected. Therefore, it is essential to figure out the exact location of the remaining Co atoms. For this purpose, backscattered electron (BSE) SEM measurements combined with EDS elemental analysis were carried out. Normally, the contrast of BSE images is related only to the atomic number of elements on the surface of the sample and is independent of morphological contrasts. When the elemental distribution of the sample's surface is not uniform, areas containing atoms with large mean atomic numbers show higher brightness than an area with atoms of low mean atomic numbers. Thus, different phases can be distinguished based on the brightness contrasts of the BSE images [30]. In the present study, the BSE images revealed secondary phases along the grain boundaries for all the doped materials. As the brightness contrast is clearer in the sample with higher cobalt content, the backscattered electron (BSE) images recorded on the ceramic sample of $x = 1.2$ were selected as examples and demonstrated in Fig. 4a. As can be clearly seen, the contrast between the grain and grain boundary makes it easy to conclude that the substance along the grain boundary can be ascribed to a secondary phase. The subsequent EDS elemental distribution map analyses (Fig. 4b–d) display clear Co element distribution areas (Fig. 4d), which in fact is exactly the secondary phase areas. Element concentration analysis on a selected dot also shows a much higher Co element concentration than that of the Al and Ca element, as shown in Fig. 4e, f. These results combining with the XRD pattern of the sample $Ca_{12}Al_{12.4}Co_{1.6}O_{33+\delta}$ displayed above, the secondary phase is most likely the starting material Co_2O_3. For the XRD patterns of $Ca_{12}Al_{14\text{-}x}Co_xO_{33+\delta}$ with $x \leq 1.2$, the absence of peaks from Co_2O_3 is probably because the Co_2O_3 contents in these samples are below the detection limits of the X-ray diffractometer.

XPS analysis

In addition, XPS measurements on Co-doped samples were used to shed light on the valence state of the Co atoms. Figure 5 displays the spectrum of the sample $Ca_{12}Al_{12.8}Co_{1.2}O_{33+\delta}$. As is well documented, in the XPS spectra of Co(II) high-spin compounds, such as CoO, there are intense shake-up satellite peaks at ~ 787.0 and 804.0 eV; whereas for the XPS spectra of low-spin Co(III) compounds, the satellite peaks are weak or missing [31]. Thus, the Co 2p XPS spectrum of the well-known mixed valence oxide Co_3O_4 is symptomatic of weak shake-up satellite structures due to the minor Co(II) component [32]. In this work, besides the two main peaks around 780.81 and 796.61 eV, two apparent satellite peaks at ~ 785.41 and ~ 802.02 eV, with intermediate intensities, can be observed in the spectrum. These satellite peaks indicate the mixed valence nature of the Co element in the $Ca_{12}Al_{12.8}Co_{1.2}O_{33+\delta}$ sample. Since the Co atoms distributed along the grain boundaries are identified to exist in the form of Co_2O_3 in the trivalent state, minor divalent Co^{2+} ions therefore are assumed to have entered into the crystal structure of $Ca_{12}Al_{14}O_{33}$ and occupy the Al sites, as the divalent high-spin Co^{2+} ions, rather than the low-spin Co^{3+} ions, are usually more readily to occupy tetrahedral sites in the crystal. This is well documented and validated by experiments and DFT calculations [33]. A representative case is that of the crystal structure of mixed valence Co_3O_4 (space group Fd$\bar{3}$ m, $a \approx 8.1$ Å) where the Co^{2+} and Co^{3+} ions show highly ordered distribution in 4-coordinated tetrahedral sites and 6-coordinated octahedral sites, respectively.

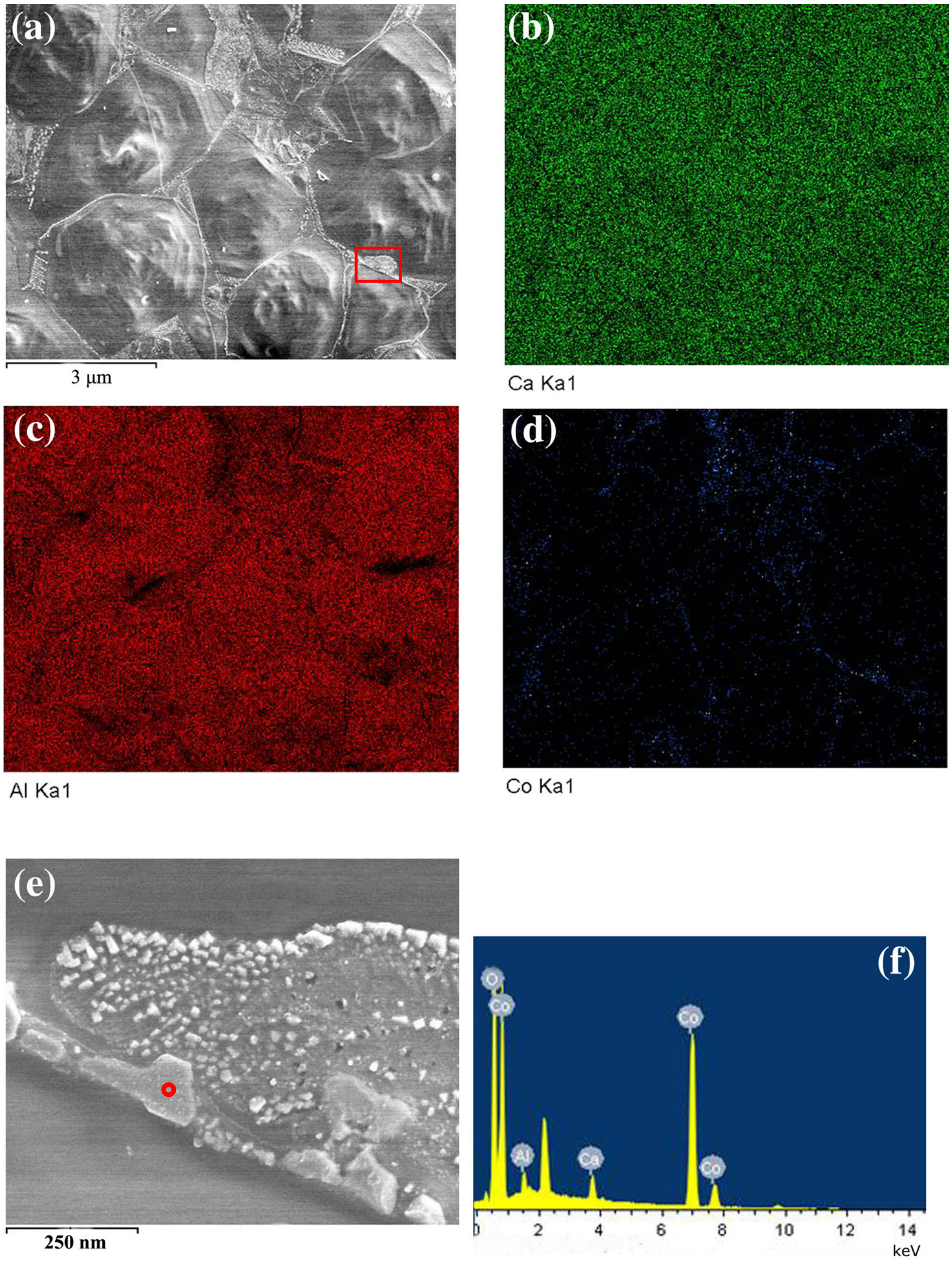

Fig. 4 SEM image (**a**) and EDS element distribution maps of Ca, Al, and Co, respectively (**b**–**d**) for the untreated $Ca_{12}Al_{12.8}Co_{1.2}O_{33+\delta}$ surface; the zoom-in picture of the area in the red rectangle in picture a (**e**); the element concentrations of the red dot in picture e (**f**), and the peak which is u-labeled corresponds to the Au element that sprayed on the surface of the ceramic pellet prior to measurements

Static lattice simulation

As previously mentioned, the refined cell parameters of $Ca_{12}Al_{14-x}Co_xO_{33+\delta}$ indicated a very narrow solid solution, and the Co ions in the mayenite structure are mainly divalent. This narrow solid solution usually relates to high defect formation energies for substitution. For the purpose of verifying, defect formation energies were then calculated using static lattice simulation technology based on combination of dopant and vacancy defect energies and lattice energies of the binary oxides, and can be simply determined from the following defect equation:

$$2CoO + 2Al_{Al}{}^{\times} \rightarrow 2Co_{Al}{}' + Al_2O_3 + V_O^{\bullet\bullet} \qquad (1)$$

i.e.,

$$\Delta H_{formation} = E(V_O{}^{\bullet\bullet}) + 2E(Co_{Al}{}') + E(Al_2O_3) - 2\,E(CoO) \qquad (2)$$

where the E(X) denotes the calculated total energy or point defect energy of the species of interest after geometric optimization.

The starting point was to reproduce the experimental crystal structure of $Ca_{12}Al_{14}O_{33}$, CoO, and Al_2O_3. The mayenite

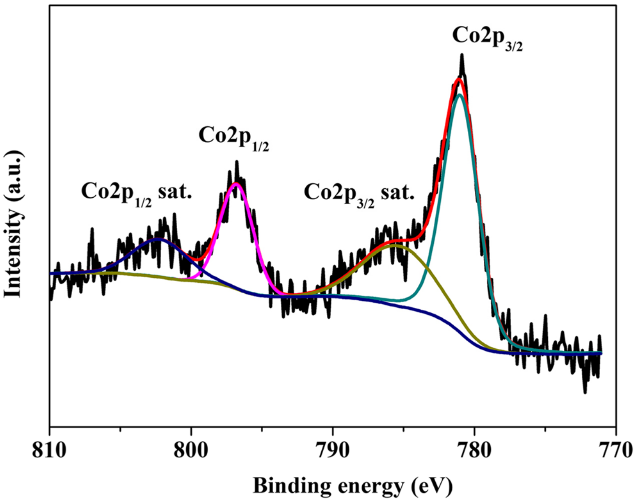

Fig. 5 The Co 2p spectra of the nominal $Ca_{12}Al_{12.8}Co_{1.2}O_{33+\delta}$ sample

structure exhibited by $Ca_{12}Al_{14}O_{33}$ material is cubic (space group $I\bar{4}\,3d$) as mentioned before, while CoO and Al_2O_3 adapt cubic and rhombohedral structure, respectively. The interatomic potentials used for these calculations are shown in Table 1. The results shown in Table 3 demonstrate that the deviations between the calculated and experimental unit cell edges and volumes are below 2%.

The final calculated formation energy for Co^{2+} ions to substitute for 3-linked tetrahedral Al2 sites, derived from Eq. (2), was ~ 6.25 eV. For comparison, the possibility of Co^{2+} ions replacing 4-linked tetrahedral Al1 sites was also investigated, which resulted in the formation energy of ~ 7.53 eV, apparently higher than that in the 3-linked case. Generally, the defect formation energy below 3.0 eV implies a relatively wide solid solution. Otherwise, it probably would have resulted in a narrow solid solution. For example, our previous work reported that for La*M*Ga_3O_7 (*M* = Ba, Sr, Ca), the highest defect formation energy of ~ 2.74 eV occurred for La substituting for Ba with about 35% of the Ba ions being replaced by La ions [34]. Recently, it has been reported that for K/Na-doped $SrSiO_3$ materials, the lowest defect formation energy when K/Na substitutes for Sr is 4.13 eV, and that the K/Na-doped $SrSiO_3$ turned out to have an extremely low range of solid solutions [35]. In the present work, the calculated defect formation energies for Co^{2+} ions replacing Al atoms explain well the narrow solid solution in $Ca_{12}Al_{14-x}Co_xO_{33+\delta}$ and verify that the Co^{2+} ions show strong preference in the 3-linked tetrahedral Al2 sites. For comparison, the defect formation energies for Co^{3+} ions substitution for Al ions were also calculated in a similar way, and the results turned out to be ~ 7.36 eV and ~ 8.95 eV for Co^{3+} ions occupying the 3-linked tetrahedral Al2 site and 4-linked tetrahedral Al2 site, respectively, apparently higher than that in the case of Co^{2+} ions.

Electrical property

The electrical properties of the $Ca_{12}Al_{14-x}Co_xO_{33+\delta}$ ceramic samples were investigated by alternating current (AC) impedance spectroscopy (IS). For AC impedance spectroscopy measurements on a ceramic sample, the different relaxation times for grains (bulk) and grain boundaries make it accessible to separate their corresponding resistance, resulting in separate semicircles in the complex impedance spectrum. Therefore, one can calculate the bulk conductivity (σ_b), grain boundary conductivity (σ_b), and the total conductivity (σ_t) once the bulk resistance (R_b), grain boundary resistance (R_g), and total resistance ($R_t = R_b + R_g$) were determined. The densities of ceramic samples for IS measurements calculated based on the Archimedes' principle are all higher than 91% of the theoretical predictions. The densities of these samples did not show regular variation as a function of Co content. The AC impedance measurements for all the samples were carried out within the temperature range of 300–950 °C.

Figure 6 displays several selected typical impedance spectra from parent $Ca_{12}Al_{14}O_{33}$ sample at various temperatures. At temperature 350 °C (Fig. 6a), the impedance complex plane plot is dominated by the semicircle arc related to grain boundary resistance (R_{gb}) response, and similar impedance spectra of $Ca_{12}Al_{14}O_{33}$ was also reported by J.T.S. Irvine et al. [18]. The inset clearly shows a small semicircle corresponding to bulk response (R_b) at high frequency. No arc related to electrode response was detected at this temperature. When the temperature reached 550 °C (Fig. 6b), besides the arcs from bulk and grain boundary responses, a small tail of Warburg-type electrode response (inclined spike which usually related with a diffusion process of ions) in the low-frequency region (< 10 Hz) with an associated large

Table 3 Calculated and experimental structural parameters of $Ca_{12}Al_{14}O_{33}$ (space group $I\bar{4}\,3d$), CoO (space group $Fm\bar{3}_m$), and Al_2O_3 (space group $R\bar{3}\,cH$)

Oxides	Parameters	Experimental	Calculated	Difference	Percent (%)
$Ca_{12}Al_{14}O_{33}$	*a*/*b*/*c* (Å)	12.04	12.092	0.052	0.43
	Volume (Å^3)	1745.34	1768.15	22.81	1.31
CoO	*a*/*b*/*c* (Å)	4.2600	4.2667	0.0067	0.16
	Volume (Å^3)	77.3087	77.6732	0.3644	0.47
Al_2O_3	*a*/*b* (Å)	4.7540	4.8555	0.1015	2.13
	c (Å)	12.9900	12.8821	− 0.1079	− 0.83
	Volume (Å^3)	254.2483	263.0148	8.7664	3.45

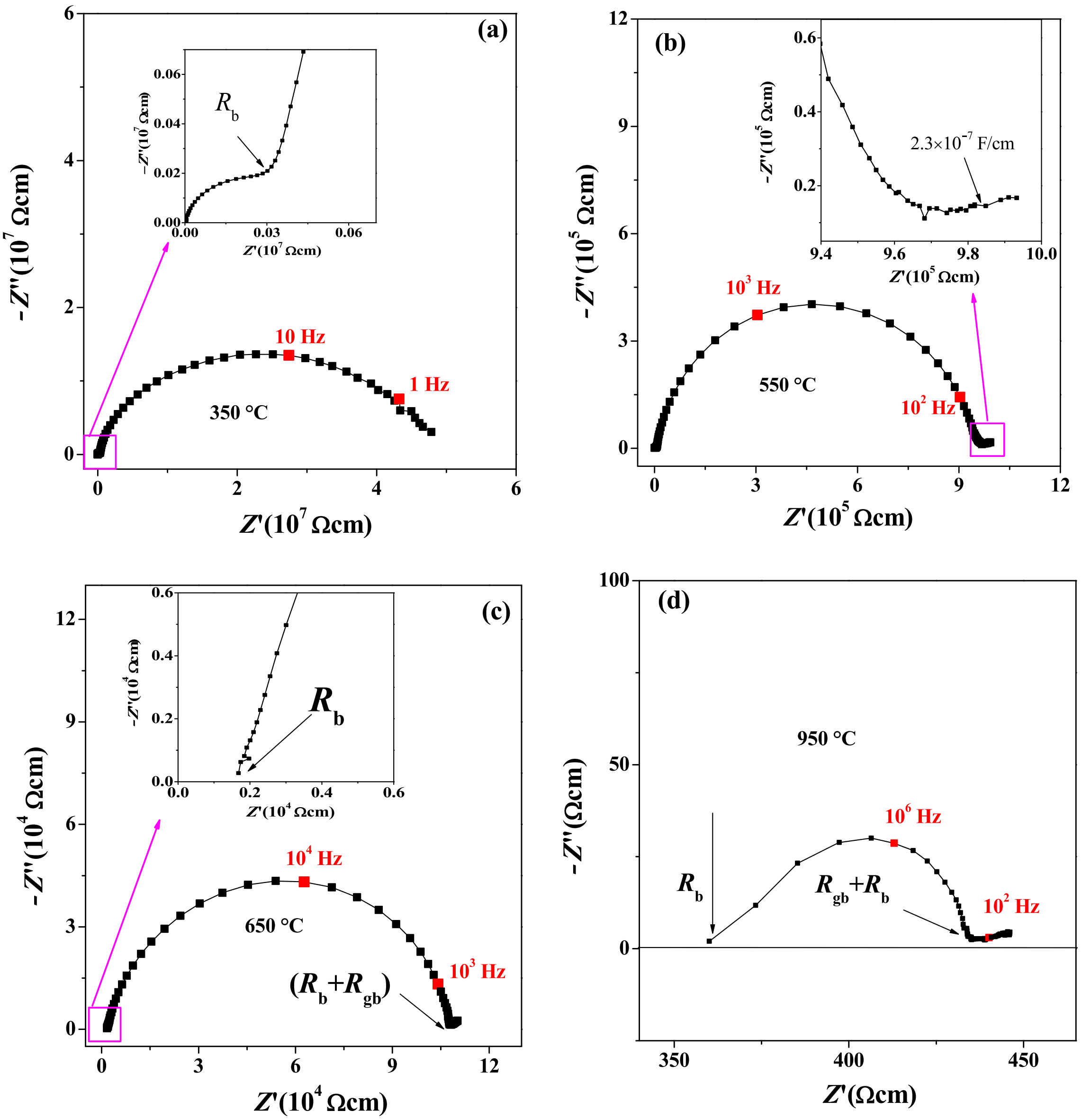

Fig. 6 **a**–**d** Complex impedance plots for $Ca_{12}Al_{14}O_{33}$ at various temperatures. Selected frequencies (Hz) marked by the red square are labeled

capacitance > 10^{-7} F/cm was observed, corresponding to the ionic conduction [36]. At temperature 650 °C (Fig. 6c), the arc from bulk response disappeared, which can be explained by the equation $2\pi f_{max}RC = 1$ where the f_{max} is the frequency at Z''_{max}, and R and C are resistance and associated capacitance of bulk, respectively [36]. Thus, when the resistance of bulk decreased with increasing temperature, the f_{max} would increase and out with respect to the frequency scale of the instrumentation (such as maximum 1×10^7 Hz here). When temperature is ≥ 950 °C, the resistance of grain boundary is much smaller than that of bulk. As can be seen in Fig. 6d, the intercept on the Z' axis at high frequency can be ascribed to the bulk resistance and is greater than 350 Ω cm, while the grain boundary resistance derived from the first semicircle on the spectra is only ~ 100 Ω cm.

Co-doping on $Ca_{12}Al_{14}O_{33}$ was revealed by complex impedance spectra to have a great effect on the electrical property, and can significantly increase the grain boundary conductivities. For illustration, Fig. 7 demonstrates the typical spectra of sample $Ca_{12}Al_{12.8}Co_{1.2}O_{33+\delta}$ recorded at various temperatures. At 350 °C, the spectrum (Fig. 7a) is composed of two severely overlapped and depressed arcs at high- and low-frequency regions related to bulk and grain boundary response, respectively, with a following small tail corresponding to electrode response arising from ionic conduction. The electrode response, however, was not observed at the same temperature for the parent material, indicating that the Co-doping can accelerate the migration of the free oxide ions in this material. Usually, a perfect semicircle with center on the real axis represents an ideal Debye type behavior corresponding to

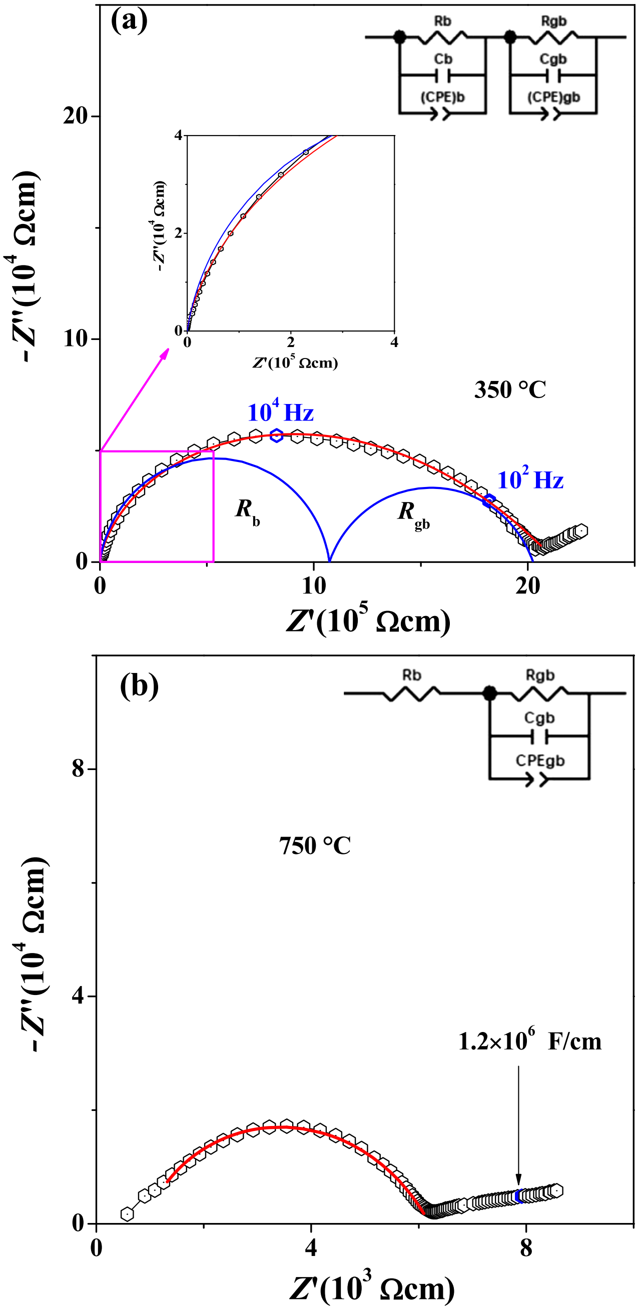

Fig. 7 **a**, **b** Complex impedance plots of the sample $Ca_{12}Al_{12.8}Co_{1.2}O_{33+\delta}$. The experimental and calculated data are shown as black open hexagons and red solid line, respectively

a single relaxation mechanism, and can be modeled through a parallel resistance-capacitance circuit. However, such perfect semicircular arcs are expected only in homogeneous materials. In ceramic systems, due to the variations in grain size, the semicircular arcs in the complex impedance plane corresponding to the grain and grain boundary effects would get inclined to the real axis with the center generally located below the real axis implying distribution of relaxation time [37, 38]. In such case, a simple parallel network model of bulk or grain boundary resistance-capacitance (R_b–C_b or R_{gb}–C_{gb}) is accepted as a poor approximation [39]. When this non-ideal frequency response is present, it is commonly accepted to employ distributed circuit elements in an equivalent circuit, and the most widely used is the constant phase element (CPE), which has a non-integer power dependence on the frequency [40]. Often a CPE is used in a model in place of a capacitor to compensate for non-homogeneity in the system. Therefore, in order to acquire the accurate resistances of bulk and grain boundary, here, equivalent circuit consisting of a serial combination of two circuits with three parallel R_i, C_i, and $(CPE)_i$ elements (R, C, and CPE represent the device resistance, capacitance, and constant phase element, respectively; i is b for bulk or gb for grain boundary) were used to model these two responses, as illustrated in the inset in the top right corner of Fig. 7a. The bulk conductivity (σ_b) and grain boundary conductivity (σ_{gb}) are calculated from R_b and R_{gb}, respectively, while the total conductivity (σ_b) is calculated from the total resistance of R_b plus R_{gb}, i.e., $R_b + R_{gb}$. The obtained R_b (~ 1.1×10^6 Ω cm) is higher than that of the un-doped $Ca_{12}Al_{14}O_{33}$ (3.21×10^5 Ω cm) at the same temperature, but the R_{gb} (~ 9.0×10^5 Ω cm) is much lower than that of the parent $Ca_{12}Al_{14}O_{33}$ (~ 4.75×10^7 Ω cm). This indicates that the substitution of Co^{2+} for Al^{3+} in the crystal structure will decrease the bulk conductivity of $Ca_{12}Al_{14}O_{33}$, which can be most likely ascribed to the reduction of free oxygen content caused by this acceptor doping, and the segregation of Co_2O_3 along the grain boundary can significantly enhance the grain boundary conduction. When the temperature is ≥ 750 °C, the semicircle corresponding to the bulk impedance diminished. This is because the bulk impedance is out respect to the frequency scale of the instrumentation, as explained for Fig. 6c with a similar phenomenon. The grain boundary impedance dominated the spectra at this temperature, as can be appreciated from Fig. 7b**.**

Figure 8 shows the bulk, grain boundary, and total conductivities of $Ca_{12}Al_{14\text{-}x}Co_xO_{33+\delta}$ ($x = 0$, 0.4, 0.8, 1.2). It can be seen that the bulk conductivities of the doped samples are not improved as we have expected, but even slightly lower than that of the parent material, especially in the low-temperature regions (Fig. 8a). A similar behavior occurred with Zn-doped $Ca_{12}Al_{14\text{-}x}Zn_xO_{33+\delta}$ materials as previously reported [18]. However, the bulk conductivities of these Co-doped materials at a given temperature are close to each other, which may be explained by the fact of close levels of Co contents in the crystal structure of those doped materials as stated before. In addition, all these doped materials have almost the same activation energy (~ 0.96 eV) which is slightly higher than that of the un-doped $Ca_{12}Al_{14}O_{33}$ (~ 0.79 eV). This activation energy increase is likely related to the local framework distortion arising from the replacement of aluminum by cobalt, and the similar case also occurred in the zinc- and/or phosphorus-doped $Ca_{12}Al_{14}O_{33}$ materials [18]. Although the bulk conduction was decreased with Co-doping, Fig. 8b shows apparently

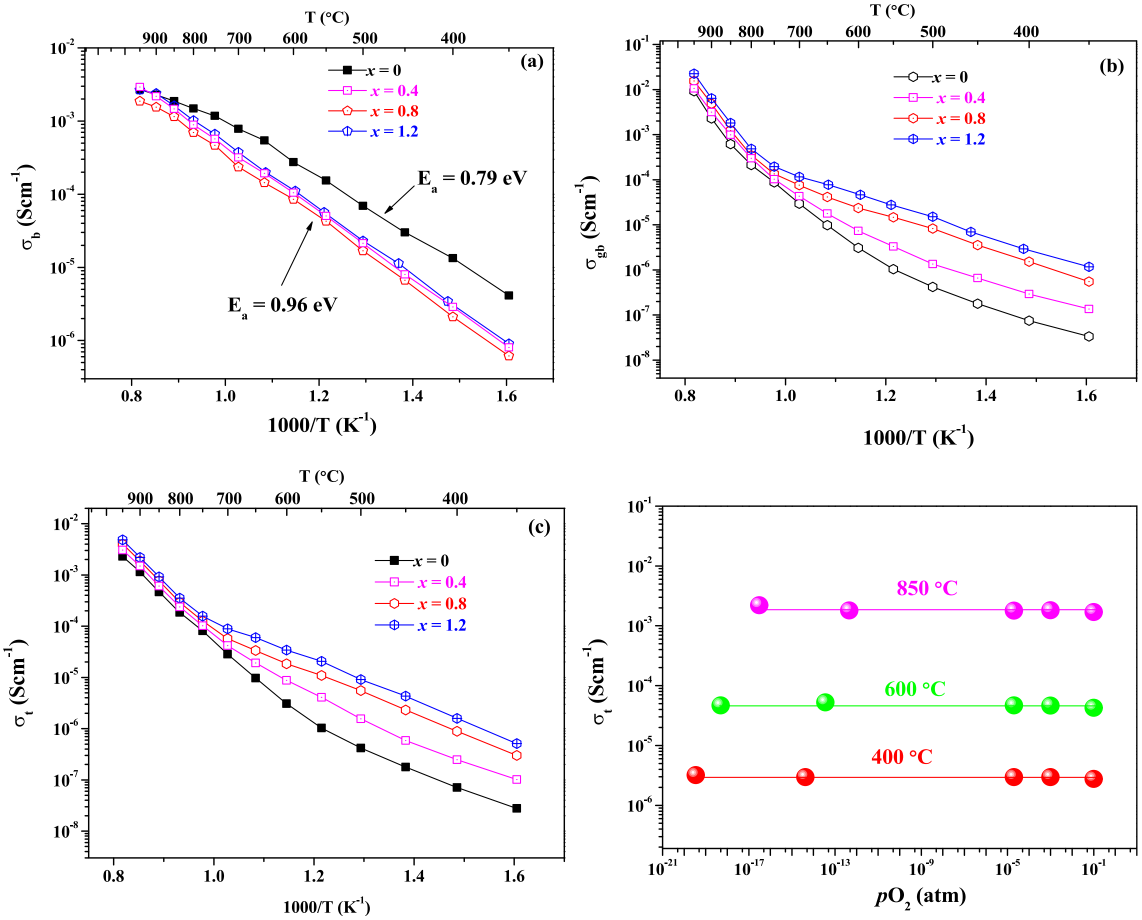

Fig. 8 **a** Bulk, **b** grain boundary, and **c** total conductivities of $Ca_{12}Al_{14-x}Co_xO_{33+\delta}$; **d** p O_2 dependence of total conductivity for the sample $Ca_{12}Al_{12.8}Co_{1.2}O_{33+\delta}$

enhances in grain boundary conductivities at temperatures ≤ 650 °C. The improvements are limited at temperatures above 700 °C. This can be explained by the fact that at low temperatures, the oxide ions transport between grains is greatly blocked at grain boundaries in the un-doped material, making the grain boundary the main limiting factor for oxide ion migration. While for the Co-doped materials the existence of Co_2O_3 along the grain boundaries can greatly reduce the blocking resistance between the grains. At elevated temperatures, the resistance of grain boundaries becomes small and is no longer the main limiting factor for oxide ion migration even for the un-doped material; therefore, the effect of Co_2O_3 segregation along grain boundaries appears to lessen the increase of conduction at grain boundaries. Figure 8c shows the enhancements in total conductivities of series $Ca_{12}Al_{12.8}Co_{1.2}O_{33+\delta}$ samples.

To verify whether there are electronic conductivities for those Co-doped materials, AC impedance measurements were performed on the $Ca_{12}Al_{12.8}Co_{1.2}O_{33+\delta}$ sample under different atmospheres with variable oxygen partial pressures between 400 and 850 °C. The results showed no apparent change in the total conductivity under variable atmospheres, as shown in Fig. 8d, indicating the pure ionic conduction nature in the Co-doped materials, and the electronic conduction, if any, was small.

Conclusion

In this work, a series of Co-doped $Ca_{12}Al_{14-x}Co_xO_{33+\delta}$ ($0 \leq x \leq 1.6$) materials were synthesized by a traditional solid-state method. Although the XRD did not detect a secondary phase for $x \leq 1.2$, the Rietveld structure refinements together with SEM, EDS and XPS technologies revealed that only a small amount of Co element (Co^{2+}) successfully substituted the 3-linked tetrahedral site Al atoms in the crystal structure of $Ca_{12}Al_{14}O_{33}$ and most of the Co atoms were distributed along the grain boundaries in the form of Co_2O_3. The high defect formation energy (~6.25 eV) calculated with a static lattice simulation technique agrees well with the narrow solid solution range for Co^{2+}/Al^{3+} in the crystal structure. The substitution of Co^{2+} for Al^{3+} ions slightly reduced the bulk conductivities for the doped materials, but apparently increased the grain boundary conductions, and without electronic conduction introduced.

Funding information This work was supported by the Guangxi Natural Science Foundation (Nos. 2017GXNSFAA198203, Nos. 2015GXNSFBA139233), National Natural Science Foundation of China (Nos. 21601040), and Guangxi Ministry-Province Jointly-Constructed Cultivation Base for State Key Laboratory of Processing for non-Ferrous Metal and Featured Materials (Nos. 14KF-9).

Compliance with ethical standards

Conflict of interest The authors declare that there are no conflicts of interest.

References

1. Brandon N, Hagen A, Dawson R, Bucheli O (2017) Solid oxide fuel cells, electrolyzers and reactors: from development to delivery–EFCF2016. Fuel Cells 17(4):414–414
2. Longo S, Cellura M, Guarino F, Ferraro M, Antonucci V, Squadrito G (2017) Life cycle assessment of solid oxide fuel cells and polymer electrolyte membrane fuel cells: a review. In Hydrogen Economy. Academic Press, pp 139–169
3. Zhang Y, Knibbe R, Sunarso J, Zhong Y, Zhou W, Shao Z, Zhu Z (2017) Recent progress on advanced materials for solid-oxide fuel cells operating below 500 °C. Adv Mater 29(48):1700132
4. Badwal SPS, Ciacchi FT (2000) Oxygen-ion conducting electrolyte materials for solid oxide fuel cells. Ionics 6(1–2):1–21
5. Yokokawa H, Sakai N, Horita T, Yamaji K, Brito ME (2005) Electrolytes for solid-oxide fuel cells. MRS Bull 30(8):591–595
6. Ishihara T (2006) Development of new fast oxide ion conductor and application for intermediate temperature solid oxide fuel cells. Bull Chem Soc Jpn 79(8):1155–1166
7. Yamamoto O, Arati Y, Takeda Y, Imanishi N, Mizutani Y, Kawai M, Nakamura Y (1995) Electrical conductivity of stabilized zirconia with ytterbia and scandia. Solid State Ionics 79(1):137–142
8. Bratton RJ (2010) Defect structure of Y_2O_3-ZrO_2 solid solutions. J Am Ceram Soc 52(4):213–213
9. Kendrick E, Slater P (2012) Battery and solid oxide fuel cell materials. Annu Rep Sect A (Inorg Chem) 108(1):424–448
10. Orera A, Slater PR (2010) New chemical systems for solid oxide fuel cells†. Chem Mater 22(3):675–690
11. Packer RJ, Skinner SJ (2010) Remarkable oxide ion conductivity observed at low temperatures in a complex superstructured oxide. Adv Mater 22(14):1613–1616
12. Lacerda M, Irvine J, Glasser F, West A (1988) High oxide ion conductivity in $Ca_{12}Al_{14}O_{33}$. Nature 332(6164):525–526
13. Boysen H, Kaiser-Bischoff I, Lerch M (2008) Anion diffusion processes in O-and N-mayenite investigated by neutron powder diffraction. Diff Fundam 8:2.1–2.8
14. Hosono H, Hayashi K, Kajihara K, Sushko PV, Shluger AL (2009) Oxygen ion conduction in 12CaO· $7Al_2O_3$: O^{2-} conduction mechanism and possibility of O^- fast conduction. Solid State Ionics 180(6–8):550–555
15. Sushko PV, Shluger AL, Hayashi K, Hirano M, Hosono H (2006) Mechanisms of oxygen ion diffusion in a nanoporous complex oxide 12CaO· $7Al_2O_3$. Phys Rev B 73(1):014101
16. Kilo M, Swaroop S, Lerch M (2009) Oxygen uptake and diffusion in mayenite. In defect and diffusion forum. Vol. 289. Trans Tech Publications, pp 511–516
17. Teusner M, De Souza RA, Krause H, Ebbinghaus SG, Belghoul B, Martin M (2015) Oxygen diffusion in mayenite. J Phys Chem C 119(18):9721–9727
18. Irvine J, West A (1990) $Ca_{12}Al_{14}O_{33}$ solid electrolytes doped with zinc and phosphorus. Solid State Ionics 40:896–899
19. Ebbinghaus SG, Krause H, Lee D-K, Janek J (2014) Single crystals of C12A7 ($Ca_{12}Al_{14}O_{33}$) substituted with 1 mol% iron. Cryst Growth Des 14(5):2240–2245
20. Maurelli S, Ruszak M, Witkowski S, Pietrzyk P, Chiesa M, Sojka Z (2010) Spectroscopic CW-EPR and HYSCORE investigations of Cu^{2+} and O^{2-} species in copper doped nanoporous calcium aluminate (12CaO· $7Al_2O_3$). Phys Chem Chem Phys 12(36):10933–10941
21. Kurashige K, Toda Y, Matstuishi S, Hayashi K, Hirano M, Hosono H (2006) Czochralski growth of 12CaO·$7Al_2O_3$ crystals. Cryst Growth Des 6(7):1602–1605
22. Yi H, Lv Y, Wang Y, Fang X, Mattick V, Xu J (2019) Ga-doped $Ca_{12}Al_{14}O_{33}$ mayenite oxide ion conductors: synthesis, defects, and electrical properties. RSC Adv 9(7):3809–3815
23. Coelho A (2007) TOPAS-Academic V4. 1. Coelho Software, Brisbane
24. Gale JD (1997) GULP: a computer program for the symmetry-adapted simulation of solids. J Chem Soc Faraday Trans 93(4):629–637
25. Gale JD, Rohl AL (2003) The general utility lattice program (GULP). Mol Simul 29(5):291–341
26. Rice WE, Hirschfelder JO (1954) Second virial coefficients of gases obeying a modified Buckingham (exp—six) potential. J Chem Phys 22(2):187–192
27. Tosi MP (1964) Cohesion of ionic solids in the Born model. In solid state physics, vol 16. Academic Press, pp 1–120
28. Denton AR, Ashcroft NW (1991) Vegard's law. Phys Rev A 43(6):3161–3164
29. Shannon RD (1976) Revised effective ionic radii and systematic studies of interatomic distances in halides and chalcogenides. Acta Crystallogr Sect A: Cryst Phys, Diffr, Theor Gen Crystallogr 32(5):751–767
30. Dilks A, Graham SC (1985) Quantitative mineralogical characterization of sandstones by back-scattered electron image analysis. J Sediment Res 55(3):347–355
31. Schenck C, Dillard J, Murray J (1983) Surface analysis and the adsorption of Co (II) on goethite. J Colloid Interface Sci 95(2):398–409
32. McIntyre N, Cook M (1975) X-ray photoelectron studies on some oxides and hydroxides of cobalt, nickel, and copper. Anal Chem 47(13):2208–2213
33. Mentré O, Kabbour H, Ehora G, Tricot GG, Daviero-Minaud S, Whangbo M-H (2010) Anion-vacancy-induced magneto− crystalline anisotropy in fluorine-doped hexagonal cobaltites. J Am Chem Soc 132(13):4865–4875
34. Xu J, Wang J, Tang X, Kuang X, Rosseinsky MJ (2017) $La_{1+x}Ba_{1-x}Ga_3O_{7+0.5x}$ oxide ion conductor: cationic size effect on the interstitial oxide ion conductivity in gallate melilites. Inorg Chem 56(12):6897–6905
35. Bayliss RD, Cook SN, Scanlon DO, Fearn S, Cabana J, Greaves C, Kilner JA, Skinner SJ (2014) Understanding the defect chemistry of alkali metal strontium silicate solid solutions: insights from experiment and theory. J Mater Chem A 2(42):17919–17924
36. Irvine JT, Sinclair DC, West AR (1990) Electroceramics: characterization by impedance spectroscopy. Adv Mater 2(3):132–138
37. Gupta P, Padhee R, Mahapatra PK, Choudhary RNP (2018) Structural and electrical characteristics of Bi2YTiVO9 ceramic. Mater Res Express 5(4):045905. https://doi.org/10.1088/2053-1591/aabe06
38. Gupta P, Padhee R, Mahapatra PK, Choudhary RNP, Das S (2018) Structural and electrical properties of Bi3TiVO9 ferroelectric

ceramics. J Alloys Compd 731:1171–1180. https://doi.org/10.1016/j.jallcom.2017.10.123

39. Popova A, Raicheva S, Sokolova E, Christov M (1996) Frequency dispersion of the interfacial impedance at mild steel corrosion in acid media in the presence of benzimidazole derivatives. Langmuir 12(8):2083–2089

40. Mcdonald JR (1987) Impedance spectroscopy: emphasizing solid materials and systems. Wiley, New York, p 16